Sensors & Actuators: A. Physical 374 (2024) 115511

Contents lists available at ScienceDirect

Sensors and Actuators: A. Physical

journal homepage: www.journals.elsevier.com/sensors-and-actuators-a-physical

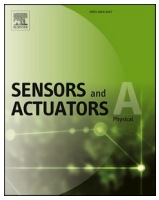

Different calibration methods for a three-component strain gauge balance to measure aerodynamic forces on airfoils

Luis Santamaría *, Mónica Galdo Vega, Manuel Garcia-Diaz, Katia María Argüelles Díaz, Jesús Manuel Fernández Oro

Fluid Mechanics Area, Department of Energy, University of Oviedo, C/Wifredo Ricart s/n, Gijon, Asturias 33204, Spain

ARTICLE INFO

Keywords:
Strain-gauge balance
Aerodynamic forces
Calibration methods
Calibration model statistics, wind tunnel testing

ABSTRACT

Wind tunnel testing of small-scale models using aerodynamic balances is a widely used and valuable methodology, particularly in pivotal sectors as wind energy and aerospace industry. Previous works introduced a novel concept of scalable, external, three-component strain gauge balance, which was further validated showing a remarkable agreement against existing experimental data. However, potential applications involving complex airfoil flow environments, or the examination of passive flow control devices are highly demanding in terms of precision, accuracy and uncertainty. This research presents a complete dataset from extensive measurements and explores different calibration methods to address these challenges. Special effort was placed on providing a detailed description of the methodology to ensure reproducibility, and the distinct requirements of each calibration method have been meticulously considered in a comprehensive comparison. The results lead to significant conclusions, indicating that exact solution linear calibration methods are adequate for some applications when suitable calibration loads are used. Nevertheless, for more advanced applications, third-order least-squares models offer the most accurate results and are thus recommended. Finally, this work identifies potential areas for further research, such as exploring double-sided calibration models and assessing the influence of model mounting on the balance behavior, which could contribute to advances in the field.

1. Introduction

Wind tunnel testing is an essential methodology in key industries such as wind energy, transportation, and aerospace. In this context, aerodynamics plays a leading role, with a direct effect in critical factors as efficiency or safety and ultimately contributing to sustainability. However, wind tunnel tests demand substantial infrastructure and specialized equipment. The necessity to maintain a high ratio between the test section and prototype sizes often leads to the use of small-scale models, which notably increases the difficulty of the measurements. Consequently, precise and well-dimensioned instrumentation becomes imperative in most situations.

The majority of conventional wind tunnel tests involve measuring aerodynamic forces. These forces are usually multidimensional, increasing the complexity of the experimental procedures required. Hence, when it is possible, adapted methodologies are used to reduce the complexity by limiting the number of relevant dimensions. Among these approaches, two-dimensional tests are the most frequently practiced.

The measurement of aerodynamic forces is mainly performed in two different ways. The first one involves integrating pressure-based measurements on the surface of the aerodynamic body using pressure tabs and a pressure scanner [1,2]. The second method utilizes an aerodynamic balance, which directly provides the forces experimented by the prototype or model [3,4].

Aerodynamic balances are complex equipment and exist in many types and sizes. Categorized by their sensor elements, they can be either strain-gauge balances or piezoelectric balances. Strain-gauge balances exhibit good precision and repeatability for steady measurements, but their accuracy is strongly limited to a relatively narrow range with the frequency response being usually an issue [5,6]. On the contrary, piezoelectric balances are able to provide a high frequency response and can capture extremely small fluctuations with accuracy, although they fail in providing steady measurements due to drift effects [7]. Additionally, depending on the intended application, balances can be internal or external. Internal balances are designed to be used inside the test section, resembling a pole in which the model is mounted [8].

* Corresponding author.
E-mail address: santamarialuis@uniovi.es (L. Santamaría).

https://doi.org/10.1016/j.sna.2024.115511
Received 6 February 2024; Received in revised form 10 May 2024; Accepted 19 May 2024
Available online 23 May 2024

Conversely, external balances are positioned outside the test section and can vary significantly in design [9,10]. External balances are most commonly employed in the measurement of airfoil performance. The diverse designs of balances, along with their multi-range and multi-dimensional characteristics tailored to specific applications, contribute to a very limited availability of standard commercial balances, particularly of the strain-gauge type. Consequently, aerodynamic balances are usually custom manufactured for each specific test.

Recently, researchers from the Fluids Mechanics Area of the University of Oviedo have developed a scalable concept for an external strain-gauge balance with notable characteristics, including different capacities for each component, ease of manufacturing and a remarkable ratio between cost and accuracy. Originally designed for investigating the galloping behavior of solar panels [11,12], this balance prototype was further validated for measuring aerodynamic forces in airfoils, obtaining a notable agreement with experimental data from existing literature [13]. More precisely, correlation coefficients of 0.9987 and 0.9893, and root-mean squared errors (RMSE) of 0.0479 and 0.1178 were obtained for the 2D drag and lift coefficients respectively, in the case of a flat plate in angles ranging from 20º to 90º. Furthermore, correlation coefficients of 0.9316 and 1.0000, and RMSE of 0.0158 and 0.0258 were achieved for the 2D drag and lift coefficients respectively, in the case of an airfoil in angles ranging -10º to 10º (region unaffected by stall hysteresis effects). Nevertheless, while the accuracy achieved was considered sufficient for validation, new potential applications in the field of airfoil aerodynamics may devise higher requirements and demands. Particularly, these applications involve the study of stalled airfoils and conducting experiments at transition Reynolds numbers, which are both crucial in the research of vertical axis wind turbines (VAWT) [14,15] and the analysis of passive flow control devices (PFCDs). PFCDs may provide significant improvements in efficiency and a considerable reduction of aerodynamic noise [16] and are commonly applied in both turbines and fans. As the typical methodologies for these kinds of studies involve comparative tests, the equipment must be able to measure a wide range of force with accuracy so that the differences between tests (which will certainly be small in the laboratory scale) are adequately characterized. Furthermore, in these types of complex flows there are additional factors related with unsteady phenomena as intermittency of the boundary layer and alternating vortex shedding which may hinder the measurements as the range of the force may experience a notable variation in a very short time. Despite this being more related with the dynamic response of the equipment, it also increases the accuracy requirements of the balance [17].

Hence, this study delves deeper into the accuracy, precision and uncertainty of the present design of external strain-gauge balance, with a particular focus on the critical factors influencing the calibration methods. Previous research has extensively explored models and methods for calibration [18,19]. However, given the great variability in balance design and associated behavior, deciding the most suitable calibration model for a specific balance and application remains as a complex task with thorough testing required. In this work, a complete and extensive design of experiments (DOE) has been carried out following the literature guidelines, allowing the application of different calibration models, and ultimately leading to a comprehensive comparison. Moreover, existing literature often lacks detailed information and explanations regarding experimental set-ups and methodologies, hindering their practical application. Therefore, in this work special emphasis has been placed on providing a detailed description of the methodology and the formal development of the models, aiming to enhance reproducibility and adopting a divulgation-oriented approach.

This work has been structured in the following way. Firstly, a detailed description of the experimental set-up is provided, offering insights into the characteristics of the balance and the calibration system. Following, various calibration models are presented in a comprehensive manner. Particularly, the studied models include exact solution of first order and least-squares models of first, second and third order. Afterwards, the design of experiments is vividly illustrated, complemented by the presentation of the measurement dataset. Subsequently, the results obtained from the application of the different models are shown. This comprises an exploration on the influence of load selection on the exact-solution linear model, testing model accuracy for the linear, quadratic, and cubic least-squares models, as well as the calculation of prediction uncertainties for each model. Finally, relevant conclusions are drawn based on the obtained results, while other important aspects are identified and proposed for future research.

2. Experimental set-up

This research was conducted in the current facilities of the Energy Department at the University of Oviedo. Fig. 1 features a complete diagram of the set-up described below.

The balance studied has been designed for small scale tests, due to its range and size. Particularly, its main application involves the measurement of aerodynamic forces in airfoils or struts in a wind tunnel environment. Hence, the balance and the calibration system are integrated into a modular appendix specifically designed to be attached to an open, small-to-medium wind tunnel. This wind tunnel can be operated at wind velocities up to 37.5 m/s, featuring a characteristic turbulence level of 0.7 % and a test section measuring $0.68 \times 0.68\ m^2$. More information can be found in [13].

The balance employed is an external, 3-component, multi-part, strain-gauge balance. Specifically, it comprises three unidirectional bending force load-cells, each equipped with two pairs of opposing strain-gauges (one pair on each side), forming a full Wheatstone bridge. These load-cells are securely fixed in a rigid structure which prevents deformations in the structural components and assures the appropriate stress transmission from the airfoil model mount to the load-cells. The airfoil model is fixed to the balance on one side and simply supported on the other side, so large deflections outside the measurement directions are prevented. In the balance frame structure, one of the load-cells is arranged vertically (with respect to the frame) and measures the horizontal force F_x, while the other two are set below, horizontally, so their combination measures both the vertical force F_y and the pitching moment M_z. Hence, the balance is primarily designed for two-dimensional experiments, which are the most common option in airfoil studies. Although the nominal range of each load-cell is 5 kg, the design of the balance permits higher loading in the vertical direction, considering that the force is divided between two of the load-cells.

As it was introduced before, this novel balance has several characteristics which differentiate it from conventional commercial balances. First, its modular design allows the use of commercially available sensors which can be replaced in case of breakage or malfunctioning, and the frame is achieved with simple geometry parts minimizing manufacturing costs. Furthermore, the design is easily scalable, either upscale or downscale, a version for smaller aerodynamic forces (using 0.78 kg load-cells) has already been manufactured and tested obtaining comparable results in its suitable range. As it was mentioned above, the balance architecture allows different ranges in the two force components, however it does use the same sensors, thus, the electrical circuitry is simplified.

The three Wheatstone bridges are fed with a stable 2.5 V voltage supplied by the Adlink USB-2401 data acquisition card, which is also

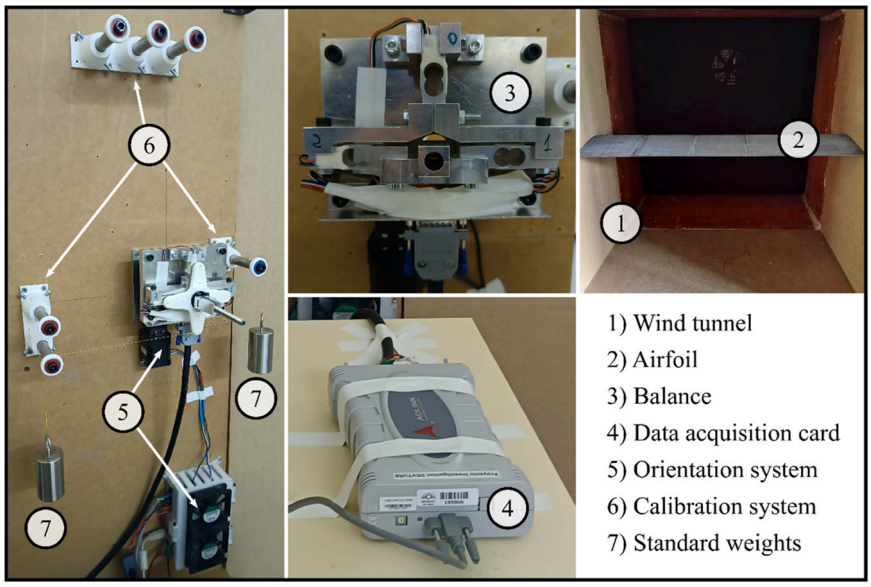

Fig. 1. Diagram of the experimental set-up used in this research.

used for the measurements. This 4-channel, 24-Bit resolution data acquisition card with built-in signal conditioning is capable of sampling rates of 2 kHz per channel.

Given the low range of the signal produced, special attention must be paid to electrical noise. In this sense some actuations have been carried out to protect the system. First, the instrumentation is isolated from the grid using a 230 V/230 V transformer, which avoids electrical noise in the supply and the ground connection. In the other end, the load cells are wired with the minimum length of cable to a DB15 connector which provides a more robust mechanical connection. The balance is grounded to avoid its metal body acting as an antenna for electromagnetic fields. As the cable length from the balance DB15 connector to the data acquisition card is about 1.8 m (a relevant length in these circumstances), special cable is needed. The cable is a 12 strand 24 AWG (which is quite a large diameter for the electronics field) insulated cooper wire, with braided metallic sheath and outside insulation. The sheath is connected to ground at the data acquisition card, so it acts like a faraday cage and protects the conductors from electromagnetic disturbances.

The balance is installed in an orientation system, resembling a CNC rotary table typically used for milling. This system allows a precise and repeatable modification of the angle of attack (AoA) by rotating the balance, while keeping both balance and prototype fixed. The system consists of a worm-gear transmission, a stepper motor and a Hall end-stop sensor, all controlled with a basic 3D printer shield board (Ramps 1.4) and an Arduino Mega.

The measurement chain and overall working principle of the balance in the wind tunnel assembly is illustrated in Fig. 2 with a block diagram.

Finally, a calibration system was designed to perform precise known loads using calibrated standard laboratory weights. These weights have a certified uncertainty smaller than 0.5 g, while ranging from 50 g to 2 kg. Note that this corresponds to the lower range of the studied balance, which is typically the most delicate in terms of calibration discrepancies. The calibration system uses a combination of polyethylene terephthalate glycol (PETG) mounts and hard steel tubes to support pulleys assembled on low-friction bearings. The pulleys allow the redirection of vertical forces exerted by the weights, in order to achieve both pure and combined loading cases, essential for a correct calibration (see Fig. 4 later).

3. Calibration methods

Modeling the behavior of a multi-component strain gauge balance can be fulfilled following two different approaches [20]. In both cases, given the multi-component nature of this type of balances, matrix

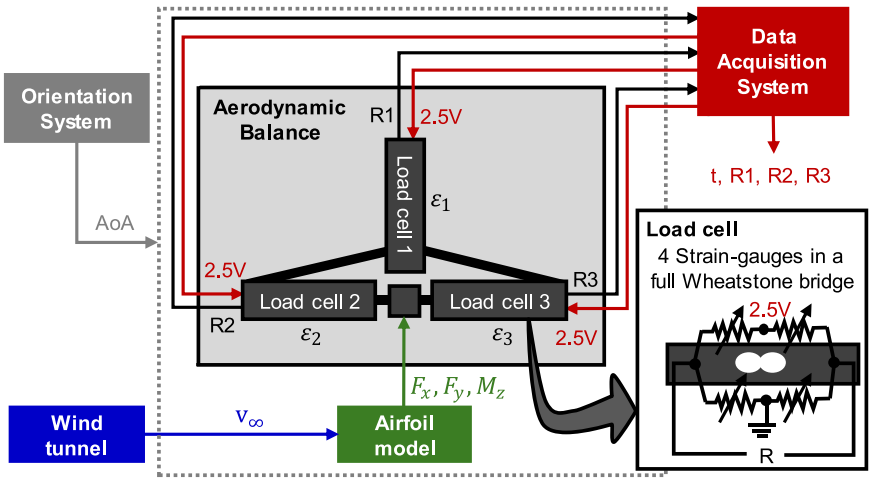

Fig. 2. Block diagram of the measurement chain and working principle of the balance in the wind tunnel assembly.

algebra is commonly employed for compactness and efficiency in the calculations. As a result, the balance behavior can be modeled through a matrix system of the following form:

$$Y = X\beta \tag{1}$$

Arguing that the forces experienced cause proportional deformation and a consequent voltage variation, the matrix containing load-cell responses R may be considered as the dependent variable Y, while the matrix comprising measured forces F, may be regarded as the independent variable X (Eq. 2). Alternatively, this relationship can be reversed as expressed in Eq. 3, assuming that the measured forces are proportional to the obtained load-cell responses. It is important to note that X and Y will share the same number of rows (representing each measurement), but their column numbers may differ based on the model's complexity, determined by the chosen number of predictor terms. As a consequence, the coefficient matrix β (also referred to as the calibration matrix) will possess a row count equal to the columns of X and a column count equal to the columns of Y.

Thus, the resulting matrix systems are:

$$R = FB \tag{2}$$

$$F = RK \tag{3}$$

where B and K represent the calibration matrixes. The decision between both ways may seem trivial for the simplest case (a linear model), as they satisfy the relation $K = B^{-1}$. However, in the case of more complex or higher-order models, the choice becomes non-trivial. The main difference resides in the retrieval of forces: while an iterative procedure is needed for the first approach, the second can be resolved with a direct computation. Hence, the first approach is usually known as the iterative method and the second as the direct method. In the literature there are examples of the use of both approaches, without a general agreement of which is superior [7,8,20]. The iterative method is more convenient and widely used for internal balances in set-ups where the calibration procedure is intricate and demands additional stages to establish the so-called tare forces. However, in this particular work, the balance used is a 3-component external balance and its set-up incorporates a loading system for precise and straightforward calibration. Hence, the first approach is chosen for streamlining the retrieval of the aerodynamic forces.

As it was explained in the previous section, the three directional components (F_1, F_2, F_3) of the studied balance correspond to the horizontal force F_x, the vertical force F_y and the pitching moment M_z, respectively. For the measurement of these forces, three load-cells with independent bridge outputs (R_1, R_2, R_3) are used. Specifically, R_1 is mainly related to the horizontal force, while R_2 and R_3 contribute to both the vertical force and pitching moment. Applying Eq. 3 to this particular balance, F is a 1×3 vector with the three force components; R is a $1\times p$ vector, with its first three terms equal to 1 (corresponding to the independent terms included in K) and the remaining terms are load-cell responses or combinations of load-cell responses. Hence, p is the number of predictor terms used in the model. And finally, K is a $3\times p$ matrix with one column for each predictor term and one row for each force component. Sometimes, as it is the present case, it is useful to rearrange, extracting the independent terms from the calibration matrix and grouping them with the cell response vector. Then, the cell responses matrix R is replaced by the matrix of "zeroed" responses ΔR, resulting in a reduction of three terms from both the number of predictor terms and calibration coefficients ($p' = p - 3$). The resulting system takes the form:

$$F = \Delta RK \tag{4}$$

Determining the appropriate level of model complexity, i.e. the number of predictor terms, involves a difficult task influenced by several factors: the specific characteristics of the balance under study, the intended purpose of the measurements, and the capabilities inherent of the calibration process. Note that as the model complexity increases, the calibration procedure becomes more demanding, requiring the application of a higher number of known loads of different types, directions, and combinations.

In addition to the problem of establishing known loads to complete a calibration procedure, the calibration matrix can be determined through two main options. The first, which involves using p' known loads to find the exact solution of the system, are known as exact solution methods (XS). The second methods, known as least-squared methods (LS) employ k points – where k is significantly larger than p' ($k >> p'$) – to provide a solution that minimizes the residual error for each point. For low complexity models, exact solution methods are more cost-effective in terms of the number of points needed. However, these methods are highly vulnerable to errors in the calibration measurements. Moreover, when the model complexity increases, careful attention must be paid to the design of the load schedule to avoid linear combinations of loads. Conversely, least-squares methods require a sizable number of points, as different loading cases (representative of the predictor terms) are needed, with several observations for each loading case. In fact, it is highly recommended to perform a suitable design of experiments (DOE) to obtain representative observations to provide an accurate regression [21]. Nevertheless, increasing the model complexity is relatively straightforward. Multiple models can be compared using the same dataset, provided it is sufficiently complete not only in terms of the number of points but also in the variety of load types and combinations. This flexibility makes least-squares methods advantageous for evaluating and comparing different models.

In this work, several calibration methods have been studied to find a solution that balances precision, across a wide range of measurements (given the demanding nature of the application), and time saving. The time factor is emphasized as it may allow calibrating before each experiment, which is a critical aspect to minimize errors coming from prototype attachments and other factors influencing the balance behavior. Particularly, an exact-solution linear model has been studied, exploring the topic of appropriate load selection. In addition, least-squares models of first, second and third orders, all derived from the same dataset, have been analyzed in depth and compared with the best exact-solution linear model.

In the following subsections, the formal development of these models is described in detail, aiming to facilitate the reproducibility of these methods for future applications and research.

3.1. Exact-solution linear model (XS-L)

The exact-solution linear model has the simplest calibration method, involving only $k = p'$ measurement points of known applied forces, with p' being equal to the number of load-cell responses (three in this case). For a single measurement, and expanding matrixes F, ΔR and K, this is expressed as follows:

$$(F_1 \quad F_2 \quad F_3) = (\Delta R_1, \Delta R_2, \Delta R_3)\begin{pmatrix} b_{1,1} & b_{1,2} & b_{1,3} \\ b_{2,1} & b_{2,2} & b_{2,3} \\ b_{3,1} & b_{3,2} & b_{3,3} \end{pmatrix} \tag{5}$$

where F_i are the measured components of the applied force, ΔR_j are the measurements of cell responses R_j minus the no-load state responses Z_j (which act as the independent terms) and $b_{j,i}$ are each of the coefficients of the calibration matrix K corresponding to linear terms.

By piling the forces and responses of the three known load measurements (k) required for the calibration, the previous system transforms into:

$$\begin{pmatrix} F_{1,1} & F_{1,2} & F_{1,3} \\ F_{2,1} & F_{2,2} & F_{2,3} \\ F_{3,1} & F_{3,2} & F_{3,3} \end{pmatrix} = \begin{pmatrix} \Delta R_{1,1} & \Delta R_{1,2} & \Delta R_{1,3} \\ \Delta R_{2,1} & \Delta R_{2,2} & \Delta R_{2,3} \\ \Delta R_{3,1} & \Delta R_{3,2} & \Delta R_{3,3} \end{pmatrix}\begin{pmatrix} b_{1,1} & b_{1,2} & b_{1,3} \\ b_{2,1} & b_{2,2} & b_{2,3} \\ b_{3,1} & b_{3,2} & b_{3,3} \end{pmatrix} \tag{6}$$

Table 1
Characteristics and assumptions of each studied model.

Method / model	Exact solution Linear (XS-L)	Least-squares Linear (LS-L)	Least-squares Quadratic (LS-Q)	Least-squares Cubic (LS-C)
Total number of calibration coefficients	9	9	27	36
Cross-product coefficients	No	No	Combined quadratic	Combined quadratic
Accounts for secondary deformations	No	No	Yes	Yes
Accounts for curvature in lower part of the range	No	No	Yes	Yes (different shape from quadratic)
Minimum number of load cases for calibration	3 non-linear combinations	Depends on balance behavior and calibration DOE (< 20 in this case)	Depends on balance behavior and calibration DOE (30 in this case)	Depends on balance behavior and calibration DOE (42 in this case)
Load cases used for calibration	3	78	78	78

The selection of loads for the three measurements is crucial due to high sensitivity of XS methods to this issue. Further discussion is later provided in Section 5.1.

3.2. Least-squares based models (LS)

Least-squares regressions are a widely employed technique in the engineering field. For these models, Eq. 4 is particularized in the following way:

$$F = \Delta R K + \epsilon \tag{6}$$

where ϵ is the matrix of residuals, containing the force residuals for each measurement. The system is solved by partial differentiation looking for the solution where the error norm of the residuals is minimum. The analysis of these residuals allows drawing important conclusions about the adequacy of the model and the balance uncertainty, which is further developed in Section 5.

Regarding the sizes and terms of the calibration and force matrixes, models with order one to three have been calibrated using a dataset of $k = 78$ known loads. Though the composition of this number is derived from the design of experiments explained in Section 4, the sample choice for calibration of the least-squares models is not trivial. In fact, as it is stated in [21] adequate sample choice is a complex topic. In other to adequately compare the different models, a sample size sufficiently large to obtain results independent from it was crucial. Depending on the order, the different calibration models achieve independence with different sample sizes. For the studied case, with this specific balance and design of experiments, linear models needed less than 20 measurement points, quadratic models at least 30 points and cubic models at least 42 points. Note that the increase in point number is not continuous but is conditioned by the design of the experiments. Despite obtaining sufficiently independent results with 42 points for the three models, a higher number was chosen to decrease the probability of type II error and the significance of every point in the calibration, as to avoid false conclusions derived from random errors in the measurements.

■ **Least-squares linear model (LS-L):**

$$\begin{pmatrix} F_{1,1} & F_{1,2} & F_{M1,3} \\ \vdots & \vdots & \vdots \\ F_{k,1} & F_{k,2} & F_{k,3} \end{pmatrix} = \begin{pmatrix} \Delta R_{M1,1} & \Delta R_{M1,2} & \Delta R_{M1,3} \\ \vdots & \vdots & \vdots \\ \Delta R_{k,1} & \Delta R_{k,2} & \Delta R_{k,3} \end{pmatrix} \begin{pmatrix} b_{1,1} & b_{1,2} & b_{1,3} \\ b_{2,1} & b_{2,2} & b_{2,3} \\ b_{3,1} & b_{3,2} & b_{3,3} \end{pmatrix} \tag{7}$$

■ **Least-squares quadratic model (LS-Q):** While the forces matrix will remain the same that in the linear model, this model also includes pure quadratic and combined quadratic predictor terms. The pure quadratic terms address non-linearities typically found in the lower part of the measuring range, while the combined terms or cross-products account for secondary deformations produced in the load-cell by those forces in different directions from the measurement one. As the number of predictor terms increases, so does the number of calibration coefficients. Hence, coefficients associated to pure quadratic predictor terms $c1_{j,i}$ and cross products $c2_{j,i}$, have been incorporated into the calibration matrix. Below, the transpose matrix ΔR^T is shown for convenience because of the large width of the predictor matrix ΔR.

$$\Delta R^T = \begin{pmatrix} \Delta R_{1,1} & \dots & \Delta R_{1,k} \\ \Delta R_{2,1} & \dots & \Delta R_{2,k} \\ \Delta R_{3,1} & \dots & \Delta R_{3,k} \\ \Delta R_{1,1}^2 & \dots & \Delta R_{1,k}^2 \\ \Delta R_{2,1}^2 & \dots & \Delta R_{2,k}^2 \\ \Delta R_{3,1}^2 & \dots & \Delta R_{3,k}^2 \\ \Delta R_{1,1}\cdot\Delta R_{2,1} & \dots & \Delta R_{1,k}\cdot\Delta R_{2,k} \\ \Delta R_{1,1}\cdot\Delta R_{3,1} & \dots & \Delta R_{1,k}\cdot\Delta R_{3,k} \\ \Delta R_{2,1}\cdot\Delta R_{3,1} & \dots & \Delta R_{2,k}\cdot\Delta R_{3,k} \end{pmatrix} \quad K = \begin{pmatrix} b_{1,1} & b_{1,2} & b_{1,3} \\ b_{2,1} & b_{2,2} & b_{2,3} \\ b_{3,1} & b_{3,2} & b_{3,3} \\ c1_{1,1} & c1_{1,2} & c1_{1,3} \\ c1_{2,1} & c1_{2,2} & c1_{2,3} \\ c1_{3,1} & c1_{3,2} & c1_{3,3} \\ c2_{1,1} & c2_{1,2} & c2_{1,3} \\ c2_{2,1} & c2_{2,2} & c2_{2,3} \\ c2_{3,1} & c2_{3,2} & c2_{3,3} \end{pmatrix} \tag{8, 9}$$

■ **Least-squares cubic model (LS-C):** This model includes additional pure cubic terms and their corresponding coefficients, denoted as $d_{j,i}$, to improve the curvature fitting in the responses. However, combined cubic terms are intentionally omitted as their presence would be indicative errors in the balance construction or looseness in joints [18]. As before ΔR^T is shown again for convenience.

$$\Delta R^T = \begin{pmatrix} \Delta R_{1,1} & \dots & \Delta R_{1,k} \\ \Delta R_{2,1} & \dots & \Delta R_{2,k} \\ \Delta R_{3,1} & \dots & \Delta R_{3,k} \\ \Delta R_{1,1}^2 & \dots & \Delta R_{1,k}^2 \\ \Delta R_{2,1}^2 & \dots & \Delta R_{2,k}^2 \\ \Delta R_{3,1}^2 & \dots & \Delta R_{3,k}^2 \\ \Delta R_{1,M1}\cdot\Delta R_{2,1} & \dots & \Delta R_{1,k}\cdot\Delta R_{2,k} \\ \Delta R_{1,M1}\cdot\Delta R_{3,1} & \dots & \Delta R_{1,k}\cdot\Delta R_{3,k} \\ \Delta R_{2,M1}\cdot\Delta R_{3,1} & \dots & \Delta R_{2,k}\cdot\Delta R_{3,k} \\ \Delta R_{1,1}^3 & \dots & \Delta R_{1,k}^3 \\ \Delta R_{2,1}^3 & \dots & \Delta R_{2,k}^3 \\ \Delta R_{3,1}^3 & \dots & \Delta R_{3,k}^3 \end{pmatrix} \quad K = \begin{pmatrix} b_{1,1} & b_{1,2} & b_{1,3} \\ b_{2,1} & b_{2,2} & b_{2,3} \\ b_{3,1} & b_{3,2} & b_{3,3} \\ c1_{1,1} & c1_{1,2} & c1_{1,3} \\ c1_{2,1} & c1_{2,2} & c1_{2,3} \\ c1_{3,1} & c1_{3,2} & c1_{3,3} \\ c2_{1,1} & c2_{1,2} & c2_{1,3} \\ c2_{2,1} & c2_{2,2} & c2_{2,3} \\ c2_{3,1} & c2_{3,2} & c2_{3,3} \\ d_{1,1} & d_{1,2} & d_{1,3} \\ d_{2,1} & d_{2,2} & d_{2,3} \\ d_{3,1} & d_{3,2} & d_{3,3} \end{pmatrix} \tag{10, 11}$$

The different assumptions and main characteristics of each model have been summarized in Table 1.

4. Design of experiments (DOE)

The design of experiments has been done following the guidelines found in [22]. Employing common practices for balance calibration, loadings were organized into series. For each series, the same procedure was followed: Firstly, ascending weights were loaded from a no-load condition until reaching the maximum weight. Afterwards, descending weights were loaded until returning to the no-load condition again. Six different series were conducted for this research, corresponding to pure loadings in each measurement component and all possible combinations of two components. Within each series, 13 points were measured including the initial and final no-load conditions, resulting in the previously mentioned 78-point measurement data set. Note that this is a single-sided procedure, involving loadings with the same sign, as the models under study do not account for asymmetrical behavior of the balance. In case of expanding the calibration method to include asymmetrical behavior, it would be necessary to perform three additional pure loading series and nine additional combined series. This would account for every possible combination of sign and component direction, adding up to a total of 18 series.

The criteria for load sign and direction were selected based on the predominant forces acting on airfoils: upward Lift, and downwind Drag. Loading in the horizontal F_x and vertical F_y force components is performed with a single standard weight, using the pulleys in the calibration system to change the direction of the forces. Loading in the moment component M_z is performed by means of a cross-shaped lever with a 5 cm arm. Pure moment loading is achieved by applying displaced, opposing horizontal forces of equal magnitude. Fig. 3 below illustrates a detailed diagram of the load cases for each series.

Raw data obtained from the balance responses in the described experiments is shown in Figs. 4 and 5. Particularly, Fig. 4 shows the zeroed mean response for each measurement point in every series, along with two additional measurements representing the initial and final no-load conditions. Similarly, Fig. 5 shows the standard deviation for each measurement point.

Fig. 4 shows a clear correspondence between the load component and the response of the orientated load-cell. For example, in the first series, loading is performed only in the horizontal force component and the reacting response is indeed that of the orientated load-cell, ΔR_1, while the other two load-cells remain unperturbed. Only the highest loads result in a slight disturbance due to secondary deformations. The responses of load-cells 1 and 3 exhibit a single-sided nature, while the response of load-cell 2 is practically identical to that of load-cell 3, exhibiting symmetry depending on whether the load is a force or a moment, respectively. Regarding the magnitude of the responses, there is an evident relationship between the load and the response, which is consistent across all three-load cells, although load-cells 2 and 3 divide the load in vertical loads.

Fig. 5 provides insight on the levels of noise found in the electrical signals. It illustrates a small magnitude of the standard deviation with respect to the mean, indicating a sufficiently clean signal for accurate measurements. In some measurement points, particularly those involving high magnitude, complex loading, a slight bump in the standard deviation is observed. This is attributed to visually imperceptible pendular oscillations in the loads, which introduce a low-frequency sinusoidal wave function centered around the mean. Note that, even working in the lower range of the load-cells, the system is highly sensitive to the loads, with the level of noise being consistently low and independent of the response magnitude.

5. Results

Using the previously presented data, different calibration methods have been studied. The main results are exposed in this section.

5.1. Influence of the load selection in exact-solution linear calibration

As mentioned before, exact solution methods are usually highly vulnerable to the quality of the chosen calibration loads, as the entire model is compelled to satisfy the specified conditions. Particularly, the deviation from the real value of the load will be extended to the whole model, causing a proportional drift in the measurements provided. The effect will be worse if a higher load is calculated from a lower load calibration point because it will magnify the error. Furthermore, there is the problem of non-linearities, which if present, will produce different magnitude of the errors depending on the proximity of the selected point to the non-linear zone. While least-squares linear methods can compensate non-linearities as they minimize the errors of every point in the sample, exact-solution linear methods only have one reference point, thus, they are unable to compensate. The most common practice is the use of the maximum value within the range to avoid extrapolation. Nevertheless, under the condition that the sensor response has been thoroughly tested across the entire range, and there are no discontinuities or prominent inflection points, alternative points apart from the maximum can be considered for calibration. The model may yield better or worse results depending on how well a calibration point represents the entire range.

In this study, the reliability of the model has been tested using loads of 2%, 10%, 20% and 40% of the full-scale (FS) capacity of the load-cell. The loads from the entire dataset, excluding those used for model calibration) were recalculated using the different calibrations, and the errors were compared to assess the accuracy. The results are depicted in Fig. 6, where the plots in each row show the errors obtained in each force component, and the columns correspond to different calibrations of the exact solution linear model (XS-L). Each marker on the plots corresponds to the error in a measurement, and the colored zones between dashed lines denote $\pm 2\sigma$ (where σ is the square root of the variance). This interval is commonly considered a valid reference for the uncertainty of the instrument. Both errors and corresponding load magnitudes have been normalized with respect to the full-scale of the load-cell. The scale used for the horizontal axis is logarithmic to better suit the distribution of the loads, however grid lines and ticks have been applied at selected load values instead of at base ten increments to facilitate the graph readability.

Notice that Fig. 6 shows comparable results among the four different calibrations. However, there are discernible trends: both the horizontal force and pitching moment exhibit a similar pattern, starting with small errors and progressively rising up as the applied force increases. In contrast, the vertical force already displays significant dispersion at low values, potentially indicating non-linearities in this component – a hypothesis supported by the results obtained in the following section. The $\pm 2\sigma$ ranges are relatively close among the four calibrations, but they do not represent a very conservative estimation of uncertainty, as certain measurements fall outside these ranges. The 2% of full-scale calibration yields the least favorable results, while the 40% calibration shows slightly better results than the other two.

To provide a summarized overview, the RMS errors for each force component have been calculated using the different calibrations and are now represented in Fig. 7.

Fig. 7 confirms the earlier observations, revealing a relatively high RMS error for the calibration of the 2 % of the full scale, especially in the horizontal and moment components. This highlights the importance of avoiding modeling the entire balance range with a significantly off-centered calibration, especially if it is performed at the lowest part of the range. This could be fixed using a piecewise calibration, dividing the range, although this would lead to an evident time consumption. Moreover, establishing the suitable range distribution would also require considerable knowledge of the balance behavior, so advanced methods might be preferable. Higher loads produce similar overall results, with the 40 % FS calibration emerging again as the most accurate in general terms. The RMS errors of this calibration are around 0.75 %.

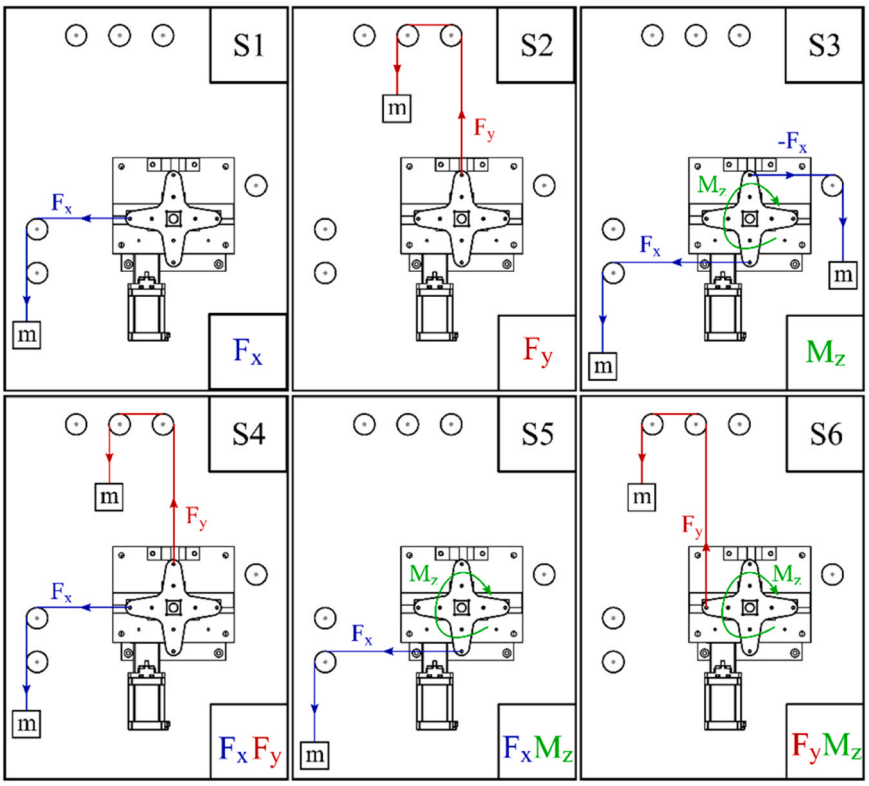

Fig. 3.. Diagram of the load cases for each series of the experiment dataset.

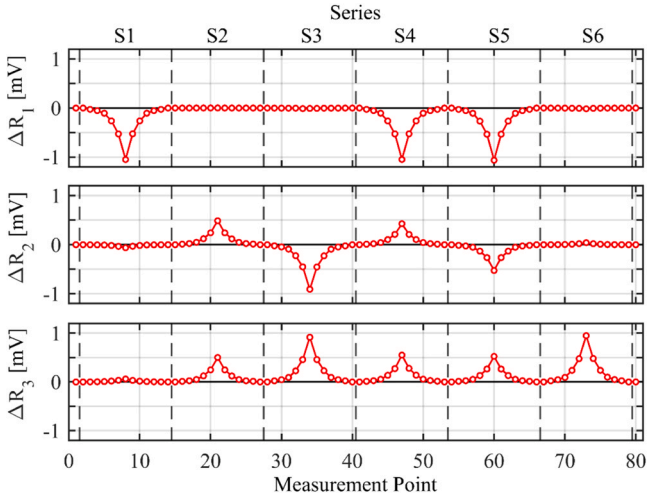

Fig. 4. Mean of the load-cell response signal of every measurement in the dataset.

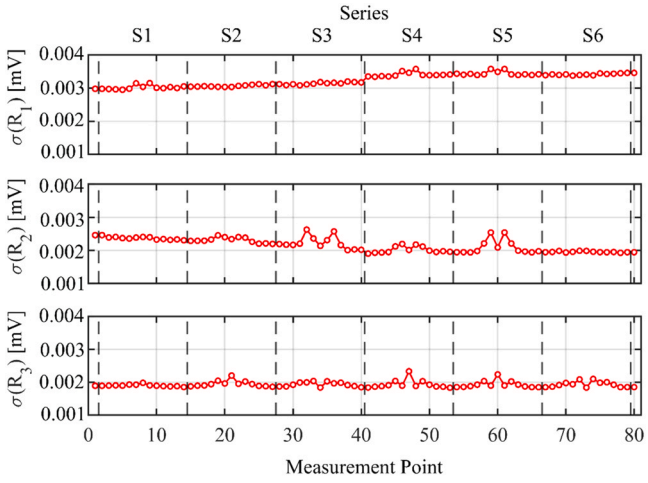

Fig. 5. Standard deviation of the load-cell response signal of every measurement in the dataset.

As a consequence, this model will be used as a reference to be compared with least-squares models later on. Its calibration matrix is presented in Table 1 below. The table also provides the percentage contribution of each predictor term to the resulting force.

The calibration matrix presented in the Table demonstrates remarkable coherence with the balance design. For the horizontal force, the predictor term $b_{1,1}$ (associated with the response of the vertically oriented load-cell) accounts for almost 100 % of the solution. In contrast, for the vertical force and pitching moment, the contribution is evenly distributed between predictor terms $b_{2,2}$ and $b_{2,3}$, and $b_{3,2}$ and $b_{3,3}$ respectively. The magnitudes of the contributing terms of the forces are rather similar, around 20 N/mV. Meanwhile, the predictor terms for the pitching moment are around 1.1 Nm/mV.

5.2. *Model adequacy in least-squares based methods*

In contrast to exact solution methods, adjusting higher-order models with least squares methods is relatively straightforward. However, increasing the model order does not necessarily guarantee improvement; one might encounter overfitting issues. Therefore, statistical testing for model adequacy is crucial to obtain a coherent and accurate solution. In this work, first, second and third-order models have been adjusted using a substantial dataset to draw conclusions that are independent of the number of data points. Nevertheless, it is worth noting that lower-order models especially, may not require as many measurement points to achieve a similarly valid solution.

Table 2 shows two statistical parameters providing insights into

model adequacy. The first is Radj, which penalizes an increase in the model order if it does not offer a significant improvement. The second parameter is the variance (σ^2) which is indicative on how well the model fits each point of the dataset.

The statistics in Table 2 suggest that, although a linear regression offers an adequate fitting, employing higher-order models can enhance the solution. In particular, the observed rise in the Radj and the reduction in variance exhibited when quadratic or cubic models are applied indicate the existence of non-linearities.

To explore this topic more in detail, the errors obtained with all the least-squares models considered (linear, quadratic and cubic) have been plotted against the magnitude of the force (Fig. 8). The values have been normalized with respect to the load-cell's full-scale range.

Substantial improvements in the force errors, especially in the horizontal force and pitching moment components, are evident when the model order is increased, especially for forces exceeding a 10 %. Although the improvement in the vertical force is not easily appreciated in this figure (due to the notable dispersion observed for the whole calibration range), it can be better identified in following results. The shared dispersion at the lower part of the calibration range for all three models suggests that this is the highest accuracy that can be achieved with this equipment. As before, a summarized result is presented by plotting the RMS error obtained for each component with every least-squares calibration model. Additionally, the results of the linear model for the exact solution at 40 % of the full-scale have been included in the figure as a reference to show the magnitude of the errors.

Fig. 9 shows a significant reduction of the errors obtained with least-squares models compared to those retrieved from the exact-solution method. Furthermore, higher-order models demonstrate a considerable improvement over linear solutions, especially in the horizontal force and pitching moment components. Interestingly, while the transition from quadratic to cubic models is not translated into a reduction in errors for both horizontal force and pitching moment, a meaningful decrease is observed in the vertical force component.

The calibration matrix and percentage contributions of the least-squares models of linear, quadratic and cubic order are shown in Tables 3, 4 and 5 respectively.

While the linear least-squares calibration practically matches the exact solution in both predictor magnitudes and contributions, the results from the quadratic and cubic calibrations provide some interesting information. Regarding the horizontal force, the magnitude of the contributions of linear, quadratic and combined terms related with any of the horizontally arranged load cells (2 and 3) is almost negligible. However, there is a slight reduction in the contribution of the linear term, which shifts towards the pure quadratic and cubic terms related to the vertically arranged load-cell. This supports the hypothesis of non-linearities in this component. Note that, if the data would better fit a lower-order model, the higher-order terms in a more complex model would be vanished. Concerning the vertical force and the pitching moment, it becomes evident that the response of the vertically oriented load cell has no influence. Additionally, there is a subtle disparity between the respective quadratic and cubic terms related with the horizontally arranged load-cells, probably tied to the direction of the force. Further tests involving different loading directions may shed some light into this aspect, but this exceeds the scope of this work. Nevertheless, as it happened with the horizontal force, the contribution of quadratic and cubic terms is non-negligible.

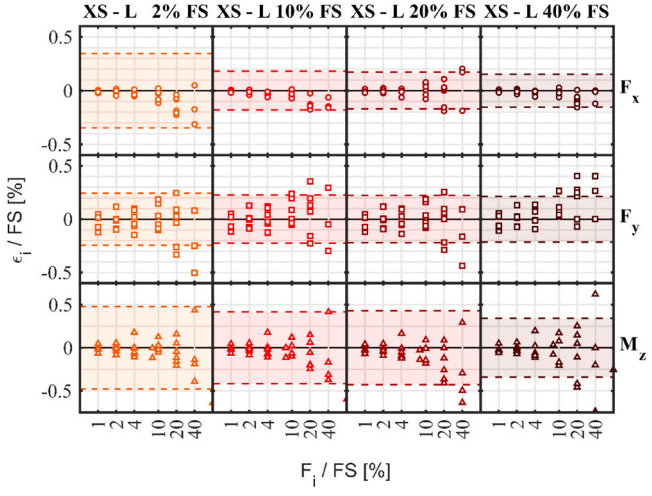

Fig. 6. Errors in the calculated forces with different calibrations of the exact solution linear model.

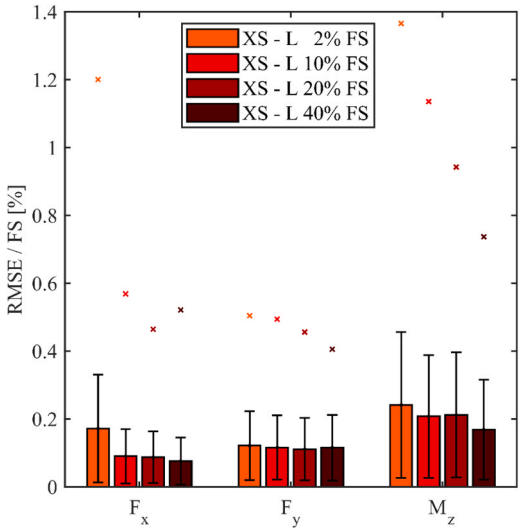

Fig. 7. Root mean square (RMS) errors in the calculated forces with different calibrations of the exact solution linear model.

5.3. Calibration uncertainty for the studied models

In this case, the $\pm 2\sigma$ estimation of the uncertainty may not be sufficiently conservative, as indicated by the previous results. Hence, alternative metrics should be employed to offer a more suitable approach. Following the procedure described in [22], a 95 % prediction interval for future observations has been calculated based on the conducted calibrations. Effectively, this interval amplitude serves as a more conservative measure for uncertainty. Eq. 12 provides the formula used for the estimation of the relative uncertainty.

$$U = 2 \cdot \frac{F + t_{0.025,(k-p')} \cdot \sqrt{\sigma^2 \cdot (1 + h_{ii})}}{F} \cdot 100 \tag{12}$$

where $t_{0.025,(k-p')}$ is the critical value of the 95% percentile of a T-student distribution with $k - p'$ degrees of freedom and h_{ii} are the diagonal elements of the H matrix presented in Eq. 13.

$$H = \Delta R \quad C\Delta R^T \tag{13}$$

where C is the variance of each of the predictor terms of the calibration matrix.

The relative uncertainties of the exact-solution linear model adjusted at 40% of the full-scale, as well as the linear, quadratic and cubic least-squares models, have been represented in Fig. 10, against the normalized calibration range. The calibration range has been divided in two intervals: from 0 to 10 in the left plots and from 10 to 40 in the right plots, to improve the visualization.

In summary, the levels of uncertainty provided by the balance are acceptable in every component, regardless of the calibration method.

Table 2
Calibration matrix of the exact-solution linear model adjusted with a 40% of the full-scale load.

	Fx		Fy		Mz	
Component	Predictor term $b_{1,j}$ [N/mV]	Contribution [%]	Predictor term $b_{2,j}$ [N/mV]	Contribution [%]	Predictor term $b_{3,j}$ [Nm/mV]	Contribution [%]
ΔR_1	-18.7263	99.8573	-0.0462	0.0004	0.1281	0.0537
ΔR_2	-0.2576	0.0824	20.0023	49.7451	-1.0940	50.3872
ΔR_3	-0.1928	0.0603	19.6937	50.2545	1.0658	49.5591

Note that this is a conservative estimation of the uncertainty level, and the calibration model is not the only source of uncertainty. Despite a special effort was undertaken to minimize uncertainty introduced by other sources, it is not possible to completely eliminate their effect. Other possible sources of uncertainty include: the temperature effect on the strain-gauges (which are properly isolated, but are still slightly sensitive), the alignment of the different systems in place (calibration and orientation), the friction and elongation of the thin technical nylon ropes used to hang the weights, and the amplification of the signal noise in the data acquisition system due to the signal conditioning.

Nonetheless, focusing on the calibration methods, the improvements offered by least-squares methods in comparison to the exact solution model are significant, particularly in demanding applications for the balance like measuring aerodynamic forces in small-scale airfoils. For the linear exact solution method, the uncertainties remain below 1 % for horizontal forces over 20 %, vertical forces over 30 % and pitching moments over 40 % of the load-cell full scale. Over 4 %, 5 % and 7 %, respectively, the uncertainties are lower than 5 %. In contrast, least-squares methods result in reduced figures, notably in the linear case (15 %, 18 %, and 30 % for 1 % uncertainty; 3 %, 4 %, and 6 % for 5 % uncertainty), and even remarkably in the cubic case (similar to the quadratic) where the uncertainties are further diminished: 5 %, 15 % and 18 % for the 1 % uncertainty and 2 %, 3 %, and 4 % for 5 % uncertainty. These results reveal that for a broad measurement range, a higher-order, least-squares calibration model becomes essential. An approximate threshold for the application of any model could be established around 20 % of the load-cell range. Thus, having a prior estimation of the magnitude and the range of the forces that are going to be measured becomes crucial for the decision-making process. Tools as analytical calculations or even tentative computational fluid dynamic (CFD) simulations can help in dimensioning the expected aerodynamic forces.

Even if an adequate estimation of the forces is not available, there are specific situations which, given the results obtained, may be susceptible to demand a least-squares calibration method, and even a higher order model. For instance, it is common that to avoid the huge infrastructure costs associated to a wind tunnel size, the scale of laboratory experiments is drastically reduced. Even correctly designing the experiments to maintain the suitable dimensionless numbers, this scale reduction potentially hinders the measurements, requiring a higher accuracy from the instrumentation. This is significantly aggravated when the aim of the tests is to study phenomena with a complex aerodynamic component as experiments subjecting an airfoil to different levels of turbulence, testing the effect of surface finish or icing conditions, or optimizing active or passive flow control devices. These are all applications in which, while a first approximation may be performed with an exact solution linear model, there is a high probability of needing a least-squares method and even a higher order model to achieve the required uncertainty levels in the measurements. Though there is a significant difference in the results, the choice of order for least-squares may be more conditioned by the availability and time-efficiency of a suitable calibration system. Despite a cubic calibration would be the most desirable regarding accuracy, its requirements in terms of load cases and associated time may discourage its use in practice. Hence, the relevance of streamlined calibration procedures and set-ups as the ones presented in this work is highlighted.

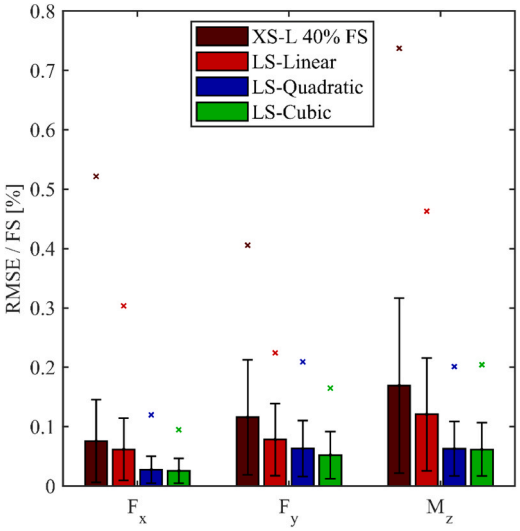

Fig. 9. RMS errors in the calculated forces least squares linear, quadratic and cubic calibrations.

Table 3
Model adecuacy statistics for first, second and third order least squares calibrations.

	Fx		Fy		Mz	
Component	Radj	σ^2	Radj	σ^2	Radj	σ^2
LS – Linear	0.99995	0.96e-3	0.99992	1.53e-3	0.99991	0.91e-5
LS – Quadratic	0.99999	0.21e-3	0.99995	1.08e-3	0.99997	0.27e-5
LS – Cubic	0.99999	0.19e-3	0.99996	0.77e-3	0.99997	0.27e-5

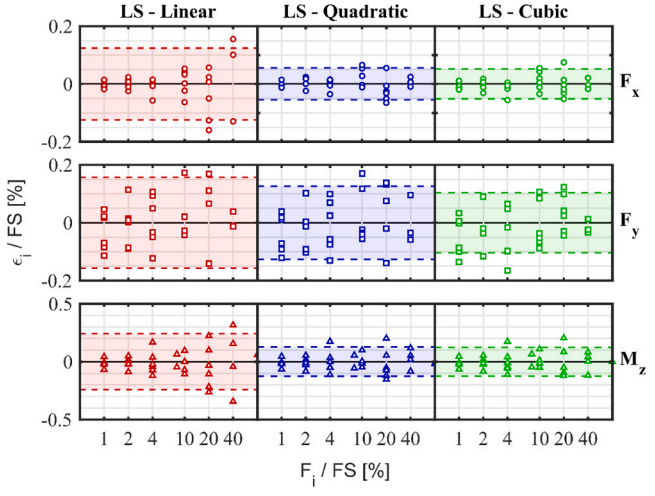

Fig. 8. Errors in the calculated forces with least squares linear, quadratic and cubic calibrations.

Table 4
Calibration matrix of the least-squares linear model.

	Fx		Fy		Mz	
	Predictor term $b_{1,j}$ [N/mV]	Contribution [%]	Predictor term $b_{2,j}$ [N/mV]	Contribution [%]	Predictor term $b_{3,j}$ [Nm/mV]	Contribution [%]
ΔR_1	-18.6720	99.8946	-0.1146	0.0009	0.1330	0.0559
ΔR_2	0.1659	0.0533	20.0734	49.6574	-1.0782	49.8530
ΔR_3	-0.1664	0.0522	19.8330	50.3417	1.0731	50.0911

Table 5
Calibration matrix of the least-squares quadratic model.

	Fx		Fy		Mz	
	Predictor term $b_{j,1}$ [N/mV]	Contribution [%]	Predictor term $b_{j,2}$ [N/mV]	Contribution [%]	Predictor term $b_{j,3}$ [Nm/mV]	Contribution [%]
ΔR_1	-18.6309	99.1039	-0.1160	0.0009	0.1384	0.0567
ΔR_2	0.2709	0.0865	20.3251	49.3650	-1.0835	48.8153
ΔR_3	-0.1853	0.0577	19.8771	49.5354	1.0703	48.6848
	Predictor term $c1_{j,1}$ [N/mV]	Contribution [%]	Predictor term $c1_{j,2}$ [N/mV]	Contribution [%]	Predictor term $c1_{j,3}$ [Nm/mV]	Contribution [%]
ΔR_1^2	0.1136	0.634	-0.0972	0.0000	0.0123	0.0000
ΔR_2^2	0.2356	0.0047	-0.2100	0.2488	-0.0298	1.2182
ΔR_3^2	-0.0954	0.0018	-0.0959	0.1197	0.0121	0.5048
	Predictor term $c2_{j,1}$ [N/mV]	Contribution [%]	Predictor term $c2_{j,2}$ [N/mV]	Contribution [%]	Predictor term $c2_{j,3}$ [Nm/mV]	Contribution [%]
$\Delta R_1 \cdot \Delta R_2$	-0.1678	0.0562	-0.0179	0.0001	-0.0300	0.0111
$\Delta R_1 \cdot \Delta R_3$	0.1582	0.0517	-0.3631	0.0014	0.0040	0.0015
$\Delta R_2 \cdot \Delta R_3$	-0.1741	0.0034	-0.5993	0.7287	-0.0171	0.7076

Table 6
Calibration matrix of the least-squares cubic model.

	Fx		Fy		Mz	
	Predictor term $b_{1,j}$ [N/mV]	Contribution [%]	Predictor term $b_{2,j}$ [N/mV]	Contribution [%]	Predictor term $b_{3,j}$ [Nm/mV]	Contribution [%]
ΔR_1	-18.7143	97.2610	0.0062	0.0000	0.1335	0.0537
ΔR_2	0.2075	0.0647	20.5377	46.6846	-1.0782	47.6507
ΔR_3	-0.1415	0.0431	20.2007	47.1155	1.0709	47.7826
	Predictor term $c1_{1,j}$ [N/mV]	Contribution [%]	Predictor term $c1_{2,j}$ [N/mV]	Contribution [%]	Predictor term $c1_{3,j}$ [Nm/mV]	Contribution [%]
ΔR_1^2	-0.2161	1.1781	0.1781	0.0000	-0.0040	0.0000
ΔR_2^2	0.2104	0.0041	0.1410	0.1563	-0.0250	1.0044
ΔR_3^2	-0.2381	0.0045	-1.8434	2.1527	0.0036	0.1463
	Predictor term $c2_{1,j}$ [N/mV]	Contribution [%]	Predictor term $c2_{2,j}$ [N/mV]	Contribution [%]	Predictor term $c2_{3,j}$ [Nm/mV]	Contribution [%]
$\Delta R_1 \cdot \Delta R_2$	-0.1437	0.0470	-0.1310	0.0005	-0.0325	0.0118
$\Delta R_1 \cdot \Delta R_3$	0.1475	0.0471	-0.4438	0.0016	0.0039	0.0015
$\Delta R_2 \cdot \Delta R_3$	0.1399	0.0027	-1.8511	2.1067	-0.0452	1.8294
	Predictor term $d_{1,j}$ [N/mV]	Contribution [%]	Predictor term $d_{2,j}$ [N/mV]	Contribution [%]	Predictor term $d_{3,j}$ [Nm/mV]	Contribution [%]
ΔR_1^3	-0.2355	1.3471	0.1497	0.0000	-0.0115	0.0000
ΔR_2^3	-0.3215	0.0004	1.5908	0.8610	0.0317	1.1537
ΔR_3^3	0.0888	0.0001	1.5754	0.9211	0.0098	0.3659

6. Conclusions

A comprehensive investigation into various calibration methods for a three-component strain gauge balance, designed for the measurement of aerodynamic forces in airfoils, has been conducted. A complete dataset, including 78 measurement points, has been obtained using a specifically designed calibration system. The formal development of the calibration methods has been widely detailed to facilitate the reproducibility of the methodology. Interesting conclusions have been obtained for both types of models under consideration.

In particular, the influence of the load selection on the exact solution methods has been analyzed. The analysis reveals that non-linearities in the lowest part of the calibration range demand calibration loads that are at least higher than 10 % of the load-cell full scale to obtain a result representative of the entire range.

Furthermore, least-squares models of first, second and third order were applied with emphasis in testing model adequacy. The results indicate that a third order model offers the highest accuracy, but with only marginal improvement over the second-order model.

The overall results, combined with a rigorous uncertainty study, suggest that linear exact-solution methods can provide accurate results for loads in the upper half of the load-cell range. However, when experiments cover a wider range, a least-squares third-order model is strongly recommended. Applications involving small-scale and the study of the effect of turbulence, surface finish, icing, or the optimization of active or passive FCDs are potentially susceptible of demanding this calibration method to provide results within acceptable uncertainty limits. Despite computational similarities between these models, the

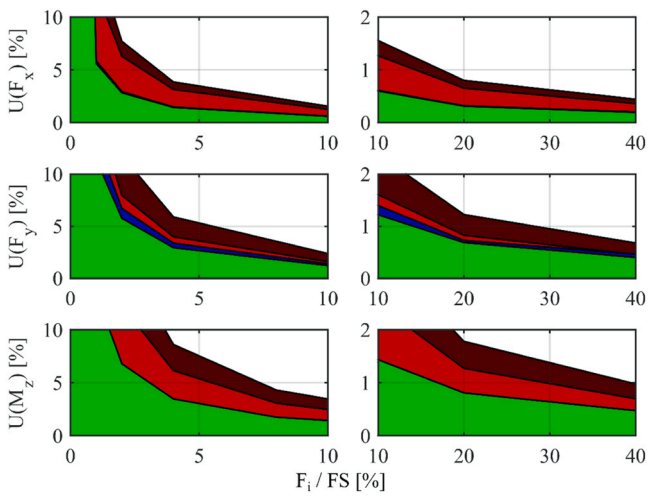

Fig. 10. T-student predicted uncertainties over the full calibration range, for the exact solution linear model adjusted with a 40% FS load (dark red) and least-squares linear (red), quadratic (blue) and cubic (green) calibration methods.

cubic least-squares model demands a significantly higher number of measurements, resulting in a notable increase in time consumption. Thus, calibrating the equipment before each experiment is severely hindered and might limit the scope of tests, highlighting the value of streamlined calibration procedures and calibration systems.

Further research is needed to determine the potential impact of prototype mounting and environmental conditions on the balance behavior. This would allow performing a third-order least-squares calibration only once, and using it in different tests, provided that the no-load state is adequately characterized.

Finally, for future research, two relevant topics have been identified. Firstly, exploring the significance of load sign in the balance behavior through double-sided calibration methods and models. Secondly, the balance response under dynamic loading consistent with the unsteady nature of the aerodynamic forces should be evaluated. This last is especially interesting because a dynamic calibration can contribute to the frequency response of the balance, allowing the study of the inherent unsteady phenomena as boundary layer detachment or vortex shedding.

CRediT authorship contribution statement

Luis Santamaría: Writing – original draft, Visualization, Software, Resources, Methodology, Investigation, Data curation, Conceptualization. **Mónica Galdo Vega:** Validation, Software, Investigation, Data curation. **Manuel Garcia-Diaz:** Software, Investigation, Conceptualization. **Katia María Argüelles Díaz:** Supervision, Resources, Project administration, Funding acquisition. **Jesús Manuel Fernández Oro:** Writing – review & editing, Visualization, Validation, Supervision, Conceptualization.

Declaration of Competing Interest

The authors declare that they have no known competing financial interests or personal relationships that could have appeared to influence the work reported in this paper.

Data availability

Data will be made available on request.

Acknowledgments

The authors wish to thank the financial support of the Spanish Ministry of Science, Innovation and Universities in reference to the Project: Efficiency improvement and noise reduction of a vertical axis wind turbine for urban environments (MERTURB) – Ref. MCINN-22-TED2021–131307B-I00. Additionally, the authors would like to acknowledge the contribution of the rest of the members of the Fluids Engineering for Renewable Energy and Sustainability (FERES) research group, as well as the hard work of the laboratory technician Germán Marcos Robredo.

References

[1] H. Kamliya Jawahar, S. Alihan Showkat Ali, M. Azarpeyvand, C.R. Ilário da Silva, Aerodynamic and aeroacoustic performance of high-lift airfoil fitted with slat cove fillers, J. Sound Vib. 479 (2020) 115347, https://doi.org/10.1016/j.jsv.2020.115347.
[2] E. Livya, S. Nadaraja Pillai, The influence of serrated trailing-edge over NACA 0020 airfoil at different turbulence intensities, Lect. Notes Mech. Eng. 2 (2023) 19–24, https://doi.org/10.1007/978-981-19-6970-6_4.
[3] A.R. Tavakolpour-Saleh, A.R. Setoodeh, M. Gholamzadeh, A novel multi-component strain-gauge external balance for wind tunnel tests: simulation and experiment, Sens. Actuators, A Phys. 247 (2016) 172–186, https://doi.org/10.1016/j.sna.2016.05.035.
[4] R.A.B. Almeida, D.C. Vaz, A.P.V. Urgueira, A.R.Janeiro Borges, Using ring strain sensors to measure dynamic forces in wind-tunnel testing, Sens. Actuators, A Phys. 185 (2012) 44–52, https://doi.org/10.1016/j.sna.2012.07.024.
[5] D.M. Ştefănescu, Strain sensitivity as selection criterion for elastic elements of force transducers: a brief review, Sens. Actuators, A Phys. 315 (2020) 1–8, https://doi.org/10.1016/j.sna.2020.112238.
[6] A.R. Tavakolpour-Saleh, M.R. Sadeghzadeh, Design and development of a three-component force/moment sensor for underwater hydrodynamic tests, Sens. Actuators, A Phys. 216 (2014) 84–91, https://doi.org/10.1016/j.sna.2014.05.001.
[7] C. Tropea, A.L. Yarin, J.F. Foss, Handbook of experimental fluid mechanics, 2007.
[8] M. DuboisSix-component strain-gage balances for large wind-tunnels., Pap. - SESA (Society Exp. Stress Anal. (1980) 401–407. https://doi.org/10.1007/bf02327141. .
[9] A.F. Molland, A five-component strain gauge wind tunnel dynamometer, Strain 14 (1978) 7–13, https://doi.org/10.1111/j.1475-1305.1978.tb00258.x.
[10] M.S. Selig, B.D. McGranahan, Wind tunnel aerodynamic tests of six airfoils for use on small wind turbines, J. Sol. Energy Eng. Trans. ASME 126 (2004) 986–1001, https://doi.org/10.1115/1.1793208.
[11] E. Martínez-García, E. Blanco-Marigorta, J. Parrondo Gayo, A. Navarro-Manso, Influence of inertia and aspect ratio on the torsional galloping of single-axis solar trackers, Eng. Struct. 243 (2021), https://doi.org/10.1016/j.engstruct.2021.112682.
[12] E. Martínez-García, E.B. Marigorta, J.P. Gayo, A. Navarro-Manso, Experimental determination of the resistance of a single-axis solar tracker to torsional galloping, Scopus 78 (2021) 519–528, https://doi.org/10.12989/SEM.2021.78.5.519.
[13] L. Santamaría, M. Galdo Vega, A. Pandal, J. González Pérez, S. Velarde-Suárez, J. M.Fernández Oro, Aerodynamic performance of VAWT airfoils: comparison between wind tunnel testing using a new three-component strain gauge balance and CFD modelling, Energies 15 (2022), https://doi.org/10.3390/en15249351.
[14] D. Holst, F. Balduzzi, A. Bianchini, B. Church, F. Wegner, G. Pechlivanoglou, L. Ferrari, G. Ferrara, C.N. Nayeri, C.O. Paschereit, Static and dynamic analysis of a NACA 0021 airfoil section at low reynolds numbers based on experiments and computational fluid dynamics, J. Eng. Gas. Turbines Power 141 (2019), https://doi.org/10.1115/1.4041150.
[15] G. Bangga, G. Hutomo, R. Wiranegara, H. Sasongko, Numerical study on a single bladed vertical axis wind turbine under dynamic stall, J. Mech. Sci. Technol. 31 (2017) 261–267, https://doi.org/10.1007/s12206-016-1228-9.
[16] Z. Zhao, D. Wang, T. Wang, W. Shen, H. Liu, M. Chen, A review: approaches for aerodynamic performance improvement of lift-type vertical axis wind turbine, Sustain. Energy Technol. Assess. 49 (2022), https://doi.org/10.1016/j.seta.2021.101789.
[17] A.R. Gorbushin, A.A. Bolshakova, Unsteady axial force measurement by the strain gauge balance, Meas. J. Int. Meas. Confed. 152 (2020) 107381, https://doi.org/10.1016/j.measurement.2019.107381.
[18] N. Ulbrich, M. ReedCalibration and data analysis recommendations for three–component moment balances. In: Proceedings of the AIAA Aviat. 2019 Forum (2019) 1–16. https://doi.org/10.2514/6.2019-3153. .
[19] R. DeLoach, N. UlbrichA comparison of two balance calibration model building methods, Collect. Tech. Pap. - In: Proceedings of the 45th AIAA Aerosp. Sci. Meet. 3 (2007) 1677–1756. https://doi.org/10.2514/6.2007-147. .
[20] N. Ulbrich, Comparison of iterative and non-iterative strain-gage balance load calculation methods, In: Proceedings of the 27th AIAA Aerodyn. Meas. Technol. Gr. Test. Conf. 2010 (2010). https://doi.org/10.2514/6.2010-4202.
[21] D.C. Montgomery. Design and Analysis of Experiments, Tenth Edition, Wiley, 2020.
[22] D.C. Montgomery, George C. Runger, Applied statistics and probability for engineers, Fifth Edition, 2011.

Luis Santamaría is a researcher and Assistant Lecturer in the Fluid Mechanics Area of the Energy Department at the University of Oviedo. He received his Ph.D. degree in Energy and Process control from the University of Oviedo in 2023. He is also B.Sc. in Mechanical Engineering and MSc in Energy Engineering. His area of expertise is experimental fluid mechanics, specifically the design and manufacturing of prototypes and set-ups for wind tunnel testing, methodology and instrumentation development and data analysis and processing. His main works are in the field of wind power and aerodynamics.

Mónica Galdo Vega is an Associate Professor in the Fluid Mechanics Area of the Energy Department at the University of Oviedo. She received her Ph.D. She received her Ph.D. in Fluids, Turbomachines and Fluid Power from the University of Oviedo in 2013. Her field of research is the experimental and numerical analysis of the flow in turbomachines, including the development of measurement systems that allow to analyze the forces generated by the fluids on the blade profiles. Her research also includes the analysis of the parameters that influence the performance of the machines by means of experimental measurements of velocity fields.

Manuel García Díaz is an Associate Professor in the Fluid Mechanics Area of the Energy Department at the University of Oviedo. He received his Ph.D. degree in Energy and Process control from the University of Oviedo in 2021. He has participated in several international projects and competitions related to industrial manufacturing, renewable energy, and biological flows. His areas of interest are ocean and wind energy and bioengineering.

Katia María Argüelles Díaz is an Associate Professor in the Fluid Mechanics Area of the Energy Department at the University of Oviedo. She received her Ph.D. degree in Physics, Fluid Dynamics and Thermal Engineering from the University of Oviedo in 2005. Her areas of expertise cover the study of fluid-dynamic behavior in fluid machines using numerical and experimental techniques, including analysis of their aeroacoustic behavior in terms of noise generation and propagation to the far field. Her research also focuses on the generation of wind energy by vertical axis turbines.

Jesús Manuel Fernández Oro is Full Professor in the Fluid Mechanics Area of the Energy Department at the University of Oviedo. He received his Ph.D. degree in Physics, Fluid Dynamics and Thermal Engineering from the University of Oviedo in 2005. His research activity is mainly focused on the fluid-dynamic study of fluid machinery, the analysis and description of turbulence and unsteady, the development and application of experimental instrumentation as well as the development of numerical models for CFD applications.